Thermodynamics of Molybdenum Trioxide (MoO3) Encapsulated in Zeolite Y

Xianghui Zhang[1], Vitaliy Goncharov[1], Cody Cockreham[1], Houqian Li[1], Junming Sun[1], Hui Sun[2], Xiaofeng Guo[1], Hongwu Xu[3], Su Ha[1], Baodong Wang[4], Yong Wang[1], and Di Wu[1]

[1]Washington State University
[2]East China University of Science and Technology
[3]Los Alamos National Laboratory
[4]National Institute of Clean and Low Carbon Energy

May 26, 2021

Abstract

Zeolites with encapsulated transition metal species are extensively applied in the chemical industry as heterogenous catalysts for favorable kinetic pathways. To elucidate the energetic insights into formation of subnano-sized molybdenum trioxide (MoO3) encapsulated/confined in zeolite Y (FAU) from constituent oxides, we performed a systematic experimental thermodynamic study using high temperature oxide melt solution calorimetry as the major tool. Specifically, the formation enthalpy of each MoO3/FAU is less endothermic than corresponding zeolite Y, suggesting enhanced thermodynamic stability. As Si/Al ratio increases, the enthalpies of formation of MoO3/FAU with identical MoO3 loading tends to be less endothermic, ranging from 61.1 ± 1.8 (Si/Al = 2.9) to 32.8 ± 1.4 kJ/mol TO2 (Si/Al = 45.6). Coupled with spectroscopic, structural and morphological characterizations, and catalytic performance tests, we revealed intricate energetics of MoO3 – zeolite Y guest – host interactions and catalytic performance governed by the phase evolutions of encapsulated MoO3.

Thermodynamics of Molybdenum Trioxide (MoO_3) Encapsulated in Zeolite Y

Xianghui Zhang [a,b], Vitaliy G. Goncharov[c,d], Cody B. Cockreham [a,b,d], Houqian Li [b], Junming Sun [b], Hui Sun[e,f], Xiaofeng Guo [a,c,g], Hongwu Xu[d], Ha Su [b], Baodong Wang[h], Yong Wang [b,i], Di Wu[a,b,f,g,*]

[a] Alexandra Navrotsky Institute for Experimental Thermodynamics, Washington State University, Pullman, Washington 99163, United States

[b] The Gene and Linda Voiland School of Chemical Engineering and Bioengineering, Washington State University, Pullman, Washington 99163, United States

[c] Department of Chemistry, Washington State University, Pullman, Washington 99163, United States

[d] Earth and Environmental Sciences Division, Los Alamos National Laboratory, Los Alamos, New Mexico 87545

[e] Petroleum Processing Research Center, East China University of Science and Technology, Shanghai 200237, China

[f] International Joint Research Center of Green Energy Chemical Engineering, East China University of Science and Technology, Shanghai 200237, China

[g] Materials Science and Engineering, Washington State University, Pullman, Washington 99163, United States

[h] National Institute of Clean-and-Low-Carbon Energy, Beijing, 102211, China

[i] Institute for Integrated Catalysis, Pacific Northwest National Laboratory, Richland, Washington 99163, United States

Corresponding Author Email:

Di Wu, *d.wu@wsu.edu*

Abstract

Zeolites with encapsulated transition metal species are extensively applied in the chemical industry as heterogenous catalysts for favorable kinetic pathways. To elucidate the energetic insights into formation of subnano-sized molybdenum trioxide (MoO_3) encapsulated/confined in zeolite Y (FAU) from constituent oxides, we performed a systematic experimental thermodynamic study using high temperature oxide melt solution calorimetry as the major tool. Specifically, the formation enthalpy of each MoO_3/FAU is less endothermic than corresponding zeolite Y, suggesting enhanced thermodynamic stability. As Si/Al ratio increases, the enthalpies of formation of MoO_3/FAU with identical MoO_3 loading tends to be less endothermic, ranging from 61.1 ± 1.8 (Si/Al = 2.9) to 32.8 ± 1.4 kJ/mol TO_2 (Si/Al = 45.6). Coupled with spectroscopic, structural and morphological characterizations, and catalytic performance tests, we revealed intricate energetics of MoO_3 – zeolite Y guest – host interactions and catalytic performance governed by the phase evolutions of encapsulated MoO_3.

Introduction

For the foreseeable future, carbon-based fuels, such as natural gas, petroleum, and biomass, will continue to be a significant part of our energy infrastructure, and interfacially engineered heterogeneous catalytic materials relying on transition metal (TM) species will continue to play a critical role in meeting our daily energy needs.[1-4] It has been demonstrated that once supported or confined, TMs, their oxide, carbide and nitrides particles exhibit promising performance with high activity and selectivity in selective conversion of methane, [5-8] low-temperature CO conversion, [9,10] selective hydrogenation/dehydrogenation, [11-14] bio-oil conversion and upgrading, [15-18] and water–gas shift reaction [19,20]. Existing literature on heterogeneous catalytic materials primarily emphasize their outstanding performance and complexity in kinetics and reaction mechanisms. Meanwhile, the rapid development of catalyst synthesis has outran the existing thermodynamic database of materials that mainly documents the thermochemical properties of homogeneous systems, such as solid solutions.[21] There is currently no systematic experimental thermodynamic data on formation energetics of interfacially supported and spatially confined/encapsulated TM particles that feature solid – solid interfaces and grain boundaries. [21] Moreover, the energetics of such particle – support or guest – host interfacial interactions, put simply, "the energetic cost of being small", is unknown. [21] The long-term goal of our group is to narrow such widening knowledge gap by carrying out thermodynamic studies on materials with interfacially stabilized subnano and nanoparticles using calorimetry as the fundamental tool. We firmly expect that such experimentally determined energetic insights will enable enhanced understanding for further development of inexpensive and more sustainable energy harvesting and conversion materials, nanostructured catalysts and sorbents using earth-abundant elements.

The recent focus of our group is on thermodynamics of zeolites with encapsulated transition metal-based particles/clusters. Zeolites are framework aluminosilicates with open microporosity constructed by corner-tetrahedron units (TO_4), in which the T atom is silicon (Si) or aluminum (Al). Substitution of Si^{4+} by Al^{3+} enables negatively charged framework structures with Brønsted acidity in addition to the Lewis acid sites. Owing to their crystalline open framework topologies and tunable surface sites, zeolite offers an ideal platform to support TM species for heterogeneous catalysis with high activity and shape selectivity.[22,23] Employing a suite of highly customized calorimeters, in collaboration with Drs Davis and Zones the Navrotsky's group pioneered research on thermodynamics of pure zeolites since 1990s, in which the cation – water – zeolite interplays of alkali and alkaline earth ion-exchanged zeolites, organic structural directing agent (OSDA) – framework interactions, formation mechanisms under hydrothermal/solvothermal synthesis, and adsorption

energetics of small molecules, such as water, CO_2, and organics, were systematically investigated. [24-41] The general conclusions are (i) dehydrated zeolites are moderately metastable compared with their dense phase assemblages by less than 15 kJ/mol per TO_2 unit, and as the framework molar volume increases, such energetic difference tends to be more significant. The energetic stability of dehydrated alkali and alkaline earth ion-exchanged aluminosilicate zeolites is function of Si/Al ratio and charge-balancing cations. More specifically, these zeolites become less stable as the Si content increases or the average ionic potential of extra-framework cations increases. (ii) Generally, hydration or adsorption of small organics is exothermic and tends to be less negative as the adsorbate loading increases. (iii) Similarly, the energetics of OSDA – framework interactions and formation energetics under hydrothermal condition suggest moderately exothermic bonding, a product of subtly balanced enthalpy and entropy factors. [24-41] These studies have laid a solid foundation for zeolite thermodynamics by enabling reliable thermochemical data on natural zeolites of geochemical importance and synthetic pure zeolites applied in the petrochemical industry as sorbents, ion-exchange media and catalysts. Nevertheless, thermodynamics of zeolites with encapsulated heterocore transition metal clusters/particles, such as oxide, carbide and/or nitride clusters, has not been systematically investigated and documented. Determination of the macroscopic thermodynamic parameters that govern the formation, stability and microscopic structures of heterocore transition metal species under zeolite encapsulation will lead to enhanced understanding of their applications in chemical engineering processes.

Recently, we reported an adsorption calorimetry study elucidating the real-time formation energetics in regeneration and thermal stability of copper oxo clusters (CuO_x) confined within copper-mordenite (Cu-MOR), a promising low-temperature methane (CH_4) conversion catalyst, in which a rich energetic landscape is projected for zeolites with different encapsulated heterocore TM species. [42] The goal of this study is to determine the formation energetics and guest – host interactions and to identify the relationships among structure, energetics, catalytic performance of the unique molybdenum (Mo) oxide–zeolite Y (MoO_3/FAU) guest–host systems, in which a transition metal oxide material, MoO_3, is encapsulated within the microporosity of zeolite Y with faujasite topology (FAU). FAU is chosen for its compositional tunability, high crystallinity, and open supercage, which enables nano-scale internal space to host MoO_3 clusters/particles. Taking advantage of a full spectrum of calorimetric capabilities in the Alexandra Navrotsky Institute for Experimental Thermodynamics (AlexInstitute) at WSU, we directly probed the enthalpies of formation and energetics of guest–host interactions employing high temperature oxide melt solution calorimetry as the major experimental tool. Coupled with inductively coupled plasma mass spectrometry (ICP-MS), *ex situ* X-ray diffraction (XRD), transmission electron microscopy (TEM), *ex situ* diffuse reflectance infrared Fourier transform spectroscopy (DRIFTS), Raman spectroscopy, catalyst evaluation, and thermal analysis using an integrated thermogravimetry–differential scanning calorimetry–mass spectrometry system (TG-DSC-MS), we elucidated the thermodynamics complexity of MoO_3 formation under zeolite Y confinement as a function of Si/Al ratio with complimentary compositional, morphological, structural, and spectroscopic insights. Further, the relations among closely balanced compositional, thermodynamic and catalytic factors were discussed.

Experimental Methods

Material Synthesis

Commercial zeolite HY samples (Alfa Aesar) with faujasite (FAU) topology were used as the starting framework materials. Ammonium molybdate tetrahydrate (Sigma-Aldrich, 99%), the Mo precursor, was introduced into all zeolite Y samples by incipient wetness impregnation (IWU). We intentionally kept the MoO_3 loading low to minimize crystal growth on the external surface of FAU. Specifically, the zeolites were pretreated in a vacuum oven at 80 °C for 4 hours. Subsequently, 1.5 mL ammonium molybdate aqueous solution (0.05 mol/L) was dripped onto the 1 g pretreated samples, followed by 1 hour sonication at room temperature. After oven-drying at 120°C overnight and calcination in a tube furnace at 600°C in air for 10 hours, the MoO_3/FAU samples were obtained. According to the Si/Al ratio (n) and MoO_3 encapsulation, the samples are labeled as$n$ FAU and MoO_3/n FAU (see **Table 1**). For example, the MoO_3-containing zeolite Y sample with Si/Al = 3.0 is named as MoO_3/3.0FAU.

Phase and Morphology Identification

Room temperature *ex situ* powder X-ray diffraction (XRD) was employed for phase identification using a Rigaku Miniflex 600 diffractometer operated at 40 kV and 15 mA with Cu Kα radiation (λ = 1.5406 Å). The XRD patterns were recorded from 5 to 60° at a step of 2° per min. The sample morphology was evaluated with transmission electron microscopy (TEM, FEI Tecnai T20, LaB_6 cathode, 200 kV) in the Franceschi Microscopy and Imaging Center at Washington State University (WSU). In each TEM experiment, a small amount of specimen was dispersed in ethanol under ultrasonication. This suspension was dropped on a carbon-coated nickel grid (200-mesh) and was further dried using infrared lamp for 20 mins.

Compositional and Thermal Analyses

The sample compositions were determined with ICP-MS (Agilent 770) and an integrated TG-DSC-MS system (Netzsch STA 449 F5 Jupiter coupled with QMS 403 D Aeolos). In the thermal analysis, the pelletized sample was placed in a Pt crucible for TG-DSC measurement from 30 to 1000 °C at 10 °C/min under N_2 flow of 50 mL/min. The gas phase product species evolved from TG-DSC were introduced to the MS via a heated capillary tube accurately controlled at 200 °C for compositional identification. We also calculated the enthalpy of dehydration of each sample based on its TG-DSC-MS data. Dehydration and phase transition are mirrored on the TG-DSC-MS curves.

Ex situ Diffuse Reflectance Infrared Fourier Transform Spectroscopy (DRIFTS)

Ex situ diffuse reflectance infrared Fourier transform spectroscopy (DRIFTS) was performed on a Nicolet iS50 FT-IR instrument from Thermo Scientific. All samples were pretreated in a 120°C oven for 4 hours to remove physi-sorbed water before DRIFTS experiments, which were performed at room temperature with data recorded from 4000 to 650 cm^{-1}.

Raman Spectroscopy

Raman spectra of all samples were collected on a Horiba LabRAM HR Raman spectrometer with a Ventus LP 532 nm laser. In each measurement, ˜ 15 mg sample was loaded into a Linkam CCR cell and the spectra were directly recorded at room temperature.

N_2 Adsorption – Desorption Full Isotherm Analysis

Brunauer-Emmett-Teller (BET) surface area pore dimension analyses were performed via N_2 adsorption – desorption full isotherm analysis at liquid nitrogen temperature (77 K or –196°C) using a commercial gas adsorption analyzer (Micromeritics 3Flex). Each sample was degassed at 300°C at the analysis port for at least 5 hours before isotherm measurement.

H_2 Temperature-Programmed Reduction (TPR)

Hydrogen (H_2) TPR experiments were carried out on a Diablo 5000A real-time gas analyzer with an Agilent 5975C MSD as the detector. Prior to the H_2 TPR analysis, each sample was pretreated *in situ* by heating to 600 °C (10°C/min) in argon flow (50 mL/min). The sample was kept at 600 °C for half an hour to remove any pre-adsorbed species. Upon cooling to 50 °C, H_2flow (25 mL/min) was introduced, meanwhile the Ar flowrate is adjusted to 25 mL/min. Subsequently, the sample analyzed was heated from 50 to 850 °C in 80 minutes in the 1 : 1 mixture of H_2 and Ar (25 mL/25 mL). The water signal is recorded for further interpretation.

Catalytic Performance Tests with Pulse Carburization of Methane (CH_4)

Pulse CH_4 carburization experiments over all MoO_3/FAU samples were also conducted on a Diablo 5000A real-time gas analyzer with an Agilent 5975C MSD as detector. Before pulse CH_4 carburization, each sample was heated from room temperature to 800 °C (10°C/min) in Ar flow (50 mL/min) followed by half an hour pre-treatment at 800 °C for desorption. The system was programed to pulse CH_4 for 10 seconds followed by 3 min Ar purge. The flow rates of CH_4 and Ar are controlled to be 30 mL/min and 50 mL/min, respectively.

High Temperature Oxide Melt Drop Solution Calorimetry

A Tian-Calvet twin microcalorimeter (Setaram Alexsys-1000) at WSU was employed for high temperature oxide melt drop solution calorimetry. The details of this methodology have been reported earlier elsewhere by Navrotsky *et. al.* [43] To measure the enthalpy of dissolution of each sample, a sample pellet (˜5 mg) was directly dropped into Alexsys-1000, which contains the solvent, lead borate ($2PbO*B_2O_3$) molten salt at 700°C under flowing compressed air at a rate of 120 mL/min. Such calorimetric measurement on each sample was repeated for at least six times. The calorimeter calibration was carried out by measuring the heat content of corundum (Al_2O_3). The enthalpies of formation and Mo oxide – zeolite Y guest – host interactions of all samples were derived using the thermodynamic cycle listed in **Table 2** . The errors are calculated as two standard deviations of the mean.

Table 1. Chemical composition, molecular weight and lattice parameter of each FAU or MoO_3/FAU sample studied on TO_2 basis.

Sample	Chemical Composition on TO_2 Basis	MW	a (Å)	BET Surface Area (m^2/g)	Specific Volume (m^3/g)	Pore Size (nm)
2.9FAU	$(SiO_2)_{0.742}$ $(Al_2O_3)_{0.13}{\cdot}0.916H_2O$	74.23	8.2906	1067.4	0.65	0.72
16.1FAU	$(SiO_2)_{0.942}$ $(Al_2O_3)_{0.03}{\cdot}0.196H_2O$	63.07	8.0297	1176.4	0.79	0.77
29.3FAU	$(SiO_2)_{0.967}$ $(Al_2O_3)_{0.017}{\cdot}0.136H_2O$	62.23	8.0424	1203.9	0.72	0.78
45.6FAU	$(SiO_2)_{0.979}$ $(Al_2O_3)_{0.011}{\cdot}0.078H_2O$	61.28	8.145	911.1	0.58	0.78
MoO_3/2.9FAU	$(MoO_3)_{0.025}$ $(SiO_2)_{0.742}$ $(Al_2O_3)_{0.13}{\cdot}0.727H_2O$	74.37	8.1581	703.1	0.44	0.72
MoO_3/16.1FAU	$(MoO_3)_{0.031}$ $(SiO_2)_{0.942}$ $(Al_2O_3)_{0.03}{\cdot}0.177H_2O$	67.24	7.9671	631.6	0.46	0.76
MoO_3/29.3FAU	$(MoO_3)_{0.027}$ $(SiO_2)_{0.967}$ $(Al_2O_3)_{0.017}{\cdot}0.138H_2O$	66.15	8.0297	1057.2	0.65	0.77
MoO_3/45.6FAU	$(MoO_3)_{0.027}$ $(SiO_2)_{0.979}$ $(Al_2O_3)_{0.011}{\cdot}0.120H_2O$	65.91	8.0424	631.6	0.43	0.77

Hosted file

`image1.emf` available at https://authorea.com/users/415965/articles/523708-thermodynamics-of-molybdenum-trioxide-moo3-encapsulated-in-zeolite-y

Figure 1. (a) Structural illustration and *ex situ* XRD patterns of zeolite Y with a faujasite-type structure (FAU),**(b)** *ex situ* XRD patterns of MoO_3/FAU, and **(c)** the a parameter of each sample as a function of Si/Al ratio. All *ex situ* XRD patterns were collected at room temperature; **(d–k)** The TEM images of all samples with their names labeled.

Results and Discussion

The compositions determined by coupled ICP-MS and TG-DSC-MS, including the formula and molecular weight of each sample on TO_2(tetrahedron unit) basis, are summarized in **Table 1.** The compositional results suggest successful introduction of MoO_3, and decreased water contents and molecular weight as

Si/Al increases (see **Table 1**). The *ex situ* XRD patterns of all FAU and MoO_3/FAU samples collected at room temperature are shown in **Figure 1a** and **b** . The XRD results confirm that all FAU samples have cubic faujasite structure belongs to the Fd3m space group, and MoO_3 encapsulation does not lead to significant disturbance of the long-range order of the frameworks. [44,45] The lattice parameter a of each sample is calculated and listed in **Table 1** (also see**Figure 1c**). For both FAU and MoO_3/FAU, as the Si/Al ratio content increases, the a parameter tends to decrease until reaching a plateau at about 8 Å. Meanwhile, MoO_3 loading results in slightly decreased a parameter by ˜1 % (see**Figure 1c**). This set of structural evidence confirms that encapsulation of MoO_3 clusters does not result in significant modification or interruption on the framework structure of zeolite Y over a wide Si/Al range. Additionally, our results also indicate that standard XRD cannot detect the encapsulated subnano-sized MoO_3 clusters, evidenced by the absence of any detectable diffraction patterns belong to MoO_3.

The TEM images of all samples are assembled in **Figure 1d–k** . All FAU samples feature octahedral configuration with sharp edged-crystal-like morphology. [46,47] Based on the TEM images, it appears that the particle size of zeolite Y in our study, spanning from 400 to 600 nm. Owing to the high thermal stability of FAU, after impregnation with Mo precursor and calcination at 600°C for 10 hours, there is no significant morphological evolution detected on all MoO_3/FAU samples. Interconnected nano-sized channels are clearly observed within these FAU crystals, which remain very well preserved after MoO_3encapsulation. We also noticed that the samples with higher Si content than that of 2.9FAU tend to feature more interconnected nanochannels. Moreover, according to the TEM images, there is no observable MoO_3 particle on the external surface of FAU with MoO_3-encapsulated. This is a strong evidence suggesting that the MoO_3 particles/clusters are dispersed within the FAU frameworks. Thus, integrating the compositional, structural and morphological results, we conclude that majority population of the MoO_3 clusters introduced are successfully encapsulated within the crystalline framework and mesoscale porosity of each FAU sample.

The N_2 adsorption – desorption isotherms of all samples are plotted in **Figure 2a** and **b** . The BET specific surface areas are 1067.4, 1176.4, 1203.9 and 911.1 m^2/g for 2.9FAU, 16.1FAU, 29.3FAU and 45.6FAU, respectively. Generally, MoO_3 encapsulation decreases the surface of FAU, and the specific areas are determined to be 703.1 m^2/g for MoO_3/2.9FAU, 631.6 m^2/g for MoO_3/16.1FAU, 1057.2 m^2/g for MoO_3/29.3FAU, and 631.6 m^2/g for MoO_3/45.6FAU. The pore size distribution plots were presented in **Figure 2c** and **d** . The common behavior is that the pore volume of each FAU sample decreases upon the introduction of MoO_3, and the pore size ranges from 0.72 to 0.78 nm (see **Table 1**). As demonstrated in the TEM images, there is nano-sized porosity/channel for each FAU or MoO_3/FAU sample. Inclusion of MoO_3 does not lead to significant channel blockage, and there is no detectable bulk MoO_3 formation resulting in significantly decreased pore volume (see **Figure 1** and **2**).

Hosted file

`image2.emf` available at https://authorea.com/users/415965/articles/523708-thermodynamics-of-molybdenum-trioxide-moo3-encapsulated-in-zeolite-y

Figure 2. N_2 adsorption – desorption isotherms of **(a)** FAU frameworks and **(b)** MoO_3/FAU measured at 77 K or -196 °C; and corresponding pore size distribution plots of **(c)** FAU frameworks and **(d)**MoO_3/FAU.

Hosted file

`image3.emf` available at https://authorea.com/users/415965/articles/523708-thermodynamics-of-molybdenum-trioxide-moo3-encapsulated-in-zeolite-y

Figure 3. (a–d) *Ex situ* DRIFTS data of all FAU and MoO_3/FAU samples. The sample names are label in each figure, and **(e)** Raman spectroscopy results of MoO_3/FAU.

The interfacial chemistry and MoO_3–FAU bonding specifics of all samples were studied by *ex situ* DRIFTS (see**Figure 3a–d**). Fundamentally, the low wavenumber absorbance of bonds within MoO_3 appears to be weak. Si/Al ratio increase leads to decreased local hydrophilicity within the micropores of zeolite Y, evidenced by clearly observed intensity decrease in peaks between 3700 and 3000 cm^{-1}, and at 1640 cm^{-1}, corresponding

to the stretching vibration of O-H groups and bending vibration of H_2O molecules, respectively. [42,48,49] More specifically, for 2.9FAU, MoO_3 encapsulation results in decreased intensity of peaks at 3675 cm^{-1} (shoulder) and 3590 cm^{-1} (shoulder) both ascribed to the stretching vibration of O-H bond of H_2O adsorbed at the Bronsted acid sites, and absorbance at 3440 (broad) cm^{-1} and 3210 cm^{-1} (broad) which are assigned to hydroxyl groups of water clusters, whereas the intensity of peak at 3740 cm^{-1} corresponding to stretching vibration of isolated silanol (Si-OH) groups does not change (**Figure 3a**).[50,51] In contrast, for the other FAU samples, the isolated silanol peak at 3740 cm^{-1} decreases upon MoO_3 introduction. In other words, the MoO_3 clusters on 2.9FAU are very likely anchored or encapsulated at the Bronsted acid sites near Al^{3+}. In contrast, for FAU samples with higher Si contents equal or higher than Si/Al = 16.1, MoO_3 tends to interact with a full spectrum of energetically distinctive sites closed to Si atoms because of low Al^{3+} concentration. Indeed, such selective binding of MoO_3 at Al^{3+} sites was also reported for encapsulation of MoO_3 in zeolites with other topologies and Si/Al ratios, such as ZSM-5.[50,51] Hence, evidence from DRIFTS suggests the presence of well-dispersed MoO_3 particles bonded near Al-OH in 2.9FAU, the sample with higher Al content and crystallinity (see **Figure 1a**), while for high silica FAU samples it is likely that there are multiple MoO_3 species experiencing intricate local chemistry with a spectrum of silanol groups and the pore structures.

The Raman spectroscopy results in **Figure 3e** , which further confirm the conclusion based on DRIFTS data by presenting a set of peaks reflecting the degree of dispersion for MoO_3 particles. Specifically, the relatively weak Raman band at ˜993 cm^{-1} is attributed to the Mo-O stretching. The presence of broad shoulder band at about 950 cm^{-1} for all MoO_3/FAU samples suggests that there are well-dispersed MoO_3 species at the vacancy defects of FAU. [52] Interestingly, for MoO_3/16.1FAU, sharp bands at ˜993, 815, and 666 cm^{-1} were observed, which indicates the existence of nano-sized crystalline particles in addition to well-dispersed α-MoO_3. [52-55] Such NPs around 1 nm are commonly seen for zeolites with 12-member rings and nano-channels, such as zeolite Y, which features super-cage and meso-scale porosity. [52-55] Considering there is no observable large MoO_3 particles residing on the external surface of all samples, from a thermodynamic perspective, majority of MoO_3 NPs are considered to be hosted in the internal space, crystalline framework and/or nano-channels, of zeolite Y. Meanwhile, we also found evidence suggesting existence of crystalline $Al_2(MoO_4)_3$ clusters within MoO_3/2.9FAU, the sample with the highest Al content, according to a weak band barely resolved at about 1045 cm^{-1}. [52,53,55] Generally, the Raman results synchronize well with the DRIFTS data, both suggesting dispersed MoO_3 particles encapsulated in the FAU frameworks.

Hosted file

`image4.emf` available at https://authorea.com/users/415965/articles/523708-thermodynamics-of-molybdenum-trioxide-moo3-encapsulated-in-zeolite-y

Figure 4. (a) H_2 TPR results and **(b)**conversion of CH_4 carburization as $CH_4$is pulsed onto MoO_3/FAU catalysts.

To reveal the influence of Si/Al ratio on the oxygen donation capability of encapsulated MoO_3 species and on MoO_3– zeolite Y interactions, H_2 TPR experiments were carried out on all MoO_3/FAU samples, in which the signal of reduction product, H_2O, was simultaneously monitored and plotted as a function of temperature in **Figure 4a** . There is a main reduction peak on all MoO_3/FAU samples studied centered at about 525 °C. Typically, this well-resolved H_2O peak is considered to be the product of MoO_3 reduction in H_2 flow forming MoO_2 and H_2O. [56-58] In addition, the slight "baseline shift" observed at temperatures higher than 525 °C probably indicates gradual further reduction of MoO_2 species. We also noticed that as the Si/Al increases the onset temperature of MoO_3 reduction varies. For MoO_3/2.9FAU, reduction initiates at ˜250 °C, while the other MoO_3-encapsulated FAU samples share an onset reduction temperature of ˜175 °C (see**Figure 4a**). This phenomenon indicates that as the framework Al content increases, the MoO_3 clusters are energetically better stabilized by the zeolite Y framework, leading to higher reduction resistance and evidenced by the decreased onset reduction temperature. In other words, the magnitudes of MoO_3 – zeolite Y interactions govern the onset reduction temperature of MoO_3 species. [56, 57] The energetics of MoO_3 encapsulation in all FAU frameworks is the topic we'll discuss in the final section of this paper. Indeed, similar phenomena were also reported for MoO_3 supported on zeolites with other topologies and Si/Al ratios. [58] We hesitate to

quantify the MoO_3 loading using H_2 TPR because of the low signal to noise ratio seen in**Figure 4a** .

Hosted file

`image5.emf` available at https://authorea.com/users/415965/articles/523708-thermodynamics-of-molybdenum-trioxide-moo3-encapsulated-in-zeolite-y

Figure 5. Product distribution of carburization reactions as CH_4 is pulsed onto MoO_3/FAU catalysts.**(a)** MoO_3/2.9FAU, **(b)**MoO_3/16.1FAU, **(c)** MoO_3/29.3FAU and **(d)** MoO_3/45.6FAU.

To elucidate the catalytic performance of encapsulated MoO_3 clusters on zeolite Y as a function of Si/Al ratio, we carried out pulse CH_4 carburization experiments on all MoO_3/FAU samples in a titration fashion, in which CH_4 was pulsed for 10 seconds followed by 3 min Ar purge. The conversion of CH_4 is plotted in**Figure 4b** against time (minute), and products distribution was recorded and presented in **Figure 5** . In general, the pulse CH_4 carburization reaction of this study is stepwise with *three distinctive stages* suggested by the CH_4 conversion and product distribution plots (see**Figure 4b** and **5**). [59] In *Stage I* , the CH_4 conversion is low, ˜10 %, which causes MoO_3 reduction and simultaneous release of CO and CO_2 as the dominate products. The hydrocarbon concentration in the evolved gas is considerably low. Variation in Si/Al ratio has significant impact on MoO_3 reduction. Specifically, in *Stage I* the initial CH_4conversion rates on 5MoO_3/2.9FAU and MoO_3/16.1FAU are only ˜10 %, while those of MoO_3/29.3FAU and MoO_3/45.6FAU are higher than 20 % (**Figure 4b**). Such low MoO_3 reduction rate observed indicates energetically stable MoO_3 particles encapsulated within MoO_3/2.9FAU and MoO_3/16.1FAU. We also noticed that during the first 6 CH_4 pulses the conversion of CH_4 remains constant for MoO_3/2.9FAU. The consistent conversion is a strong evidence suggesting the presence of uniformly monodispersed MoO_3 clusters/particles as the catalytic sites. However, for MoO_3/16.1FAU, the CH_4 conversion increases continuously as the first 5 pulses incremental CH_4 doses. Such evidence indicates that a significant portion of the MoO_3 species on MoO_3/16.1FAU are probably not uniformly distributed compared with MoO_3 clusters anchored in 2.9FAU as suggested by the Raman data. It also reflects that the local chemical environment of MoO_3 clusters/particles are complex with a series of different binding sites as suggested by DRIFTS. Subsequently, as soon as reaching the maximum CH_4conversion at about 6 to 7 pulses, *Stage II* – carburization of MoO_3 species initiates. In *Stage II* , the conversion of CH_4 stays high accompanied with high H_2 production, while the MS intensities of CO and CO_2 become low, with gradually fading hydrocarbon intensity. The final stage, *Stage III* , is MoO_3catalytic site deactivation, in which the CH_4 conversion rate gradually fades, unlike carburization in *Stage II* , the MS signal intensities of the major products, C_2H_4 and C_6H_6, systematically decreases (see**Figure 5**). The maximum CH_4 conversion of each sample is 23.5 % for MoO_3/2.9FAU, 44.2 % for MoO_3/16.1FAU, 53.8% for MoO_3/29.3FAU and 57.8% for MoO_3/45.6FAU. According to **Figure 4** and **5** , it is obvious that the formation of targeted product, C_6H_6, does not increase as the CH_4 conversion increases, which implies the undesired coke formation reactions are kinetically more favorable. We also notice that the C_6H_6 synthesis on MoO_3/2.9FAU features the least negative fading slope during deactivation (see **Figure 4b**). Such phenomena were also observed in C_6H_6 synthesis using Mo/ZSM-5 catalysts, in which poorly dispersed large Mo_2C particles at high loading promote the deactivation processes. For instance, employing site-sensitive probes, Vollmer *et. al.* found that coke tended to form on large Mo_2C particles, a product of sintering of loosely bonded MoO_3 precursor on ZSM-5. Similarly, Ding *et. al.* figured out that the well-dispersed MoC_x species enabled high selectivity toward C_6H_6, whereas sintering of MoC_x led to formation of larger particles, resulting in severe coke formation. Therefore, energetically stabilized Mo species with uniform distributed particle sizes are needed for catalytic CH_4 carburization with high selectivity towards C_6H_6 synthesis with low degree of coking.

Hosted file

`image6.emf` available at https://authorea.com/users/415965/articles/523708-thermodynamics-of-molybdenum-trioxide-moo3-encapsulated-in-zeolite-y

Figure 6. The thermal analysis results of FAU **(a)** TG,**(b)** DSC, **(c)** MS (m/z=18), and **(d)** (m/z=32); and MoO_3/FAU **(e)** TG, **(f)** DSC,**(g)** MS (m/z=18), and **(h)** (m/z=32) with N_2 flow at 50 mL/min from

30 to 1000°C.

The TG-DSC-MS thermal analysis results are plotted in **Figure 6** . The DTG and DDSC data are presented in **Figure 7** and **8** . Each sample features a single-step dehydration followed by calorimetric events that do not lead to observable weight loss. Specifically, the TG-DSC-MS results of FAU are relatively straightforward (**Figure 6a** –**d** , and **7a** and **c**). All FAU samples present a single stage weight loss due to dehydration centered at about 145 °C, after which the TG-DSC-MS, DTG and DDSC profiles are nearly featureless. The total weight losses for FAU samples range from 20.3 % for 2.9FAU to 1.7 % for 45.6FAU decreasing as the Si/Al or hydrophobicity increases. According to the DSC peak areas and corresponding weight loss the dehydration enthalpies are endothermic, 67.9 ± 2.1 kJ/mol water for 2.9FAU, 97.0 ± 0.8 kJ/mol water for MoO_3/16.1FAU, 109.8 ± 3.9 kJ/mol water for 29.3FAU, and 176.1 ± 4.0 for 45.6FAU (**Table 4**). According to the XRD patterns in **Figure 9a** , all FAU samples maintain their framework structure, with 2.9FAU exhibiting noticeable partial degradation.

Hosted file

`image7.emf` available at https://authorea.com/users/415965/articles/523708-thermodynamics-of-molybdenum-trioxide-moo3-encapsulated-in-zeolite-y

Figure 7. The differential TG (DTG) **(a)** FAU and**(b)** MoO_3/FAU, and differential DSC (DDSC) results of **(c)** FAU and **(d)** MoO_3/FAU with N_2 flow at 50 mL/min from 30 to 1000°C.

Hosted file

`image8.emf` available at https://authorea.com/users/415965/articles/523708-thermodynamics-of-molybdenum-trioxide-moo3-encapsulated-in-zeolite-y

Figure 8. The differential DSC (DDSC) profiles of **(a)**MoO_3/2.9FAU (713 °C), **(b)**MoO_3/16.1FAU (450, 645 °C),**(a)** MoO_3/29.3FAU (450, 645°C), and **(d)** MoO_3/45.6FAU with N_2 flow at 50 mL/min from 30 to 1000°C.

For all MoO_3/FAU samples dehydration (concluded at temperatures below 300 °C) is responsible for the major weight loss. The desorbed water is 17.3 % for MoO_3/2.9FAU, 4.5 % for MoO_3/16.1FAU, 3.7 % for MoO_3/29.3FAU, and 3.2 % for MoO_3/45.6FAU by weight percentage (see **Figure 6e** and **7b**). According to the TG-DSC traces, the enthalpies of dehydration ($\Delta H_{\text{del,l}}$) are 75.6 ± 3.8 kJ/mol water for MoO_3/2.9FAU, 107.9 ± 1.7 kJ/mol water for MoO_3/16.1FAU, 99.4 ± 2.9 kJ/mol water for MoO_3/29.3FAU, and 98.5 ± 3.9 for MoO_3/45.6FAU. Interestingly, although there is no significant weight loss signal on the TG profiles from 300 to 900°C for all samples, a pair of broad endothermic calorimetric peaks are observed centered at about 450 and 645°C on the DSC curves of MoO_3/16.1FAU, MoO_3/29.3FAU, and MoO_3/45.6FAU (**Figure 6f** and **7d**). It is noticed that although the signals of these two peaks appear to be poorly resolved on the DSC curve MoO_3/45.6FAU, the DDSC trace clearly present the trends of two endothermic peaks at about 450 and 645 °C (see**Figure 7** and **8d**). The endothermic peak at ˜450 °C is very likely due to phase transition from β-MoO_3 clusters to α-MoO_3 particles, suggested by Brezesinski *et. al* . [60] The endothermic heat effects suggest the α-MoO_3 particles are likely energetically metastable compared with the β-MoO_3 clusters encapsulated in zeolite Y under the thermal analysis condition. On the other hand, considering the melting point of bulk MoO_3 (802°C) and "melting point depression" – a common phenomenon seen for confined solid-state guest species, the second endothermic DSC peak at about 645 °C is likely due to melting of encapsulated subnano MoO_3.[35,61] Indeed, we have documented similar decreased solid – liquid phase transition temperature in an earlier study on confinement of organic solid in mesoporous silicas with different pore dimensions. [35] Additionally, according to a study by Spevack *et. al.* , it is also possible that thermal reduction of MoO_3 to Mo oxides with oxidation states lower than 6+, from Mo^{6+} to Mo^{4+} takes place in nonoxidative environments. [62] However, this is not observed here, supported by the absence of oxygen signal (m/z=32) in thermal analysis (**Figure 6h**). We also noticed that the endothermic DSC peak at ˜450 °C appears to be absent for MoO_3/2.9FAU. We attribute that it is probably because the strong MoO_3 – framework interactions on Al-rich 2.9FAU thermodynamically hinder the unfavorable phase transition of

encapsulated MoO_3 from amorphous to nanocrystalline. Surprisingly, a sharp exothermic peak is observed on the DSC curve of MoO_3/29.3FAU at about 930°C, associated with significant weight loss as much as ˜ 4.0 %. Based on the *ex situ* XRD patterns (see**Figure 9**) suggesting completely amorphous phase for MoO_3/29.3FAU after this exothermic peak, we conclude that at ˜930 °C after melting recorded at about 645 °C, the Mo oxide species evaporate, and escape the zeolite Y framework leading to eventual collapse of framework structure. The coexistence of exothermic DSC peak and weight loss reflecting vaporization of Mo oxide species highlights the strong guest – host interactions between encapsulated MoO_3 clusters and zeolite. For MoO_3/2.9FAU, other than the endothermic calorimetric peak at ˜715 °C suggesting MoO_3 melting, a broad exothermic peak close to 1000 °C is seen on its DSC curve. This broad peak is indicative of partial phase degradation, confirmed by the XRD patterns of post DSC analysis sample (see **Figure 9b**), suggesting MoO_3/2.9FAU is partially amorphized. Such intricate guest – host interactions between transition metal oxide clusters and zeolites were also seen in our study on copper (Cu) oxo cluster (CuO_x) encapsulated in mordenite (MOR), a low-temperature methane conversion catalyst, in which decomposition of CuO_x were recorded at about 915 °C. Although decomposition of CuO_x liberates oxygen, resulting in a sharp exothermic DSC peak, the MOR framework remained intact. [42]

Hosted file

`image9.emf` available at https://authorea.com/users/415965/articles/523708-thermodynamics-of-molybdenum-trioxide-moo3-encapsulated-in-zeolite-y

Figure 9. *ex situ* XRD patterns of **(a)** FAU,**(b)** MoO_3/FAU, and (c) MoO_3/2.9FAU with various MoO_3 loading, 5 %, 10 % and 15 %, treated at 1000 oC in N_2 flow at 50 mL/min.

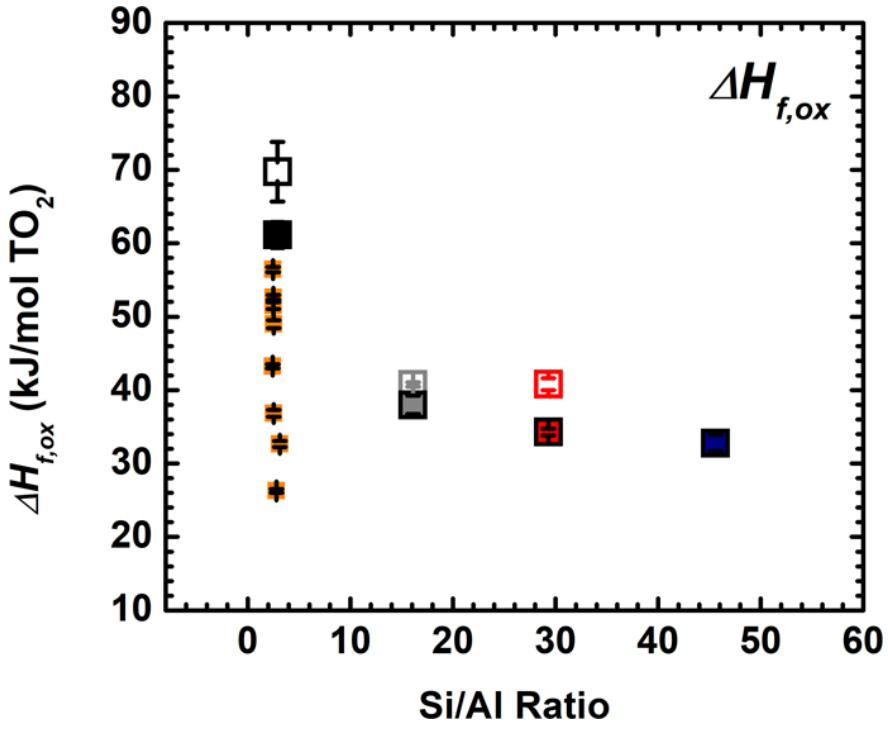

Figure 10. Enthalpies of formation from constituent oxides (SiO_2, Al_2O_3 and MoO_3) at 25 °C (per TO_2) of all FAU and MoO_3/FAU samples. Enthalpies of formation data (orange squares) of ion-exchanged zeolite Y with the same Si/Al ratio (Si/Al ˜ 2.8) documented by Yang and Navrotsky in 2000 are also presented. [31]

Table 2. Thermochemical cycle to calculate the enthalpies of formation (per TO_2) at 25 °C of FAU and MoO_3/FAU samples from their constituent oxides and elements.

$x{\cdot}(SiO_2)_y{\cdot}(Al_2O_3)_z{\cdot}nH_2O$ (s, 25 °C) ? $xMoO_3$ (soln., 700 degC) + $ySiO_2$ (soln., 700 degC) + zAl_2O_3 (soln., 700 degC) + nH_2O (g, 700
MoO_3 (s, 25 °C) ? MoO_3 (soln., 700 degC)
SiO_2 (s, 25 °C) ? SiO_2 (soln., 700 degC)
Al_2O_3 (s, 25 °C) ? Al_2O_3 (soln., 700 degC)
H_2O (l, 25 °C) ? H_2O (g, 700 degC)
Mo (s, 25 °C) + $3/2O_2$ (g, 25 °C) ? MoO_3 (s, 25 degC)
Si (s, 25 °C) + O_2 (g, 25 °C) ? SiO_2 (s, 25 degC)
2Al (s, 25 °C) + $3/2O_2$ (g, 25 °C) ? Al_2O_3 (s, 25 degC)
$(MoO_3)_x{\cdot}(SiO_2)_y{\cdot}(Al_2O_3)_z{\cdot}nH_2O$ (s, 25 °C) ?$(MoO_3)_x$*$(SiO_2)_y$*$(Al_2O_3)_z$ (s, 25 degC) + nH_2O (l, 25 degC)
$(MoO_3)_x{\cdot}(SiO_2)_y{\cdot}(Al_2O_3)_z$ (s, 25 °C) ? $xMoO_3$ (soln., 700 degC) + $ySiO_2$ (soln., 700 degC) + zAl_2O_3 (soln., 700 degC)
$\Delta H_{ds,correct} = \Delta H_{10} = \Delta H_1$ - $n\Delta H_5$ -ΔH_9
$xMoO_3$ (s, 25 °C) + $ySiO_2$ (s, 25 °C) + zAl_2O_3 (s, 25 °C) ? $(MoO_3)_x$*$(SiO_2)_y$*$(Al_2O_3)_z$ (s, 25 degC)
$\Delta H_{f,ox} = \Delta H_{11} = x[?]H_2 + y[?]H_3 + z[?]H_4$ - $[?]H_{10}$
$xMoO_3$ (s, 25 °C) + $ySiO_2$ (s, 25 °C) + zAl_2O_3 (s, 25 °C) ? $(MoO_3)_x$*$(SiO_2)_y$*$(Al_2O_3)_z$ (s, 25 degC)
$\Delta H_{f\text{-}el} = \Delta H_{13} = x[?]H_6 + y[?]H_7 + z[?]H_8 + \Delta H_{11}$
$xMoO_3$ (s, 25 °C) + $(SiO_2)_y{\cdot}(Al_2O_3)_z$ (s, 25 °C) ? $(MoO_3)_x$*$(SiO_2)_y$*$(Al_2O_3)_z$ (s, 25 degC)
$\Delta H_{inter} = \Delta H_{13} = \Delta H_{12,\ MoO3/FAU} - \Delta H_{12,\ FAU} - x\ \Delta H_6$

Table 3. Enthalpies of drop solution for constituent oxides and water in molten lead borate at 700 °C and their enthalpies of formation from elements at 25 °C.

Oxide	ΔH_{ds} **(kJ/mol)**	$\Delta H_{f,el}$ **(kJ/mol)**
Corundum (Al_2O_3)	107.4 ± 0.2 [43]	-1675.7 ± 1.3 [63]
Molybdenum trioxide (MoO_3)	-17.8 ± 0.4 [this work]	-745.2 ± 0.4 [63]
Quartz (SiO_2)	39.4 ± 0.4 [43]	-910.7 ± 1.0 [63]
Water (H_2O)	68.9 ± 0.1 [63]	-285.8 ± 0.1 [63]

The enthalpies of formation all FAU and MoO_3/FAU samples from constituent oxides ($\Delta H_{f,ox}$) and elements ($\Delta H_{f,el}$) at 25 °C are determined from their enthalpies of drop solution (ΔH_{ds}) with the thermodynamic cycle presented in **Table 2** and **3** . The enthalpies of drop solution (ΔH_{ds}) in molten lead borate at 700 °C and their enthalpies of formation from oxides ($\Delta H_{f,ox}$) and elements

Table 4. Enthalpies of drop solution (ΔH_{ds}) and formation enthalpies from oxides ($\Delta H_{f,ox}$) and elements ($\Delta H_{f,el}$) at 25 °C (per TO_2) of all samples. The dehydration enthalpies of each sample relative to liquid water ($\Delta H_{deh,l}$) and enthalpies of interactions (ΔH_{inter}) are also listed.

Sample	ΔH_{ds} **(kJ/mol)**	$\Delta H_{f,ox}$ **(kJ/mol)**	$\Delta H_{f,el}$ **(kJ/mol)**	$\Delta H_{deh,l}$ **(kJ/mol H_2O)**	ΔH_{inter} **(kJ/mol MoO_3)**
2.9FAU	50.3 ± 4.0	69.7 ± 4.1	-822.1 ± 2.0	67.9 ± 2.1	N/A
16.1FAU	19.0 ± 0.3	40.8 ± 0.3	-865.7 ± 0.2	97.0 ± 0.8	N/A
29.3FAU	13.6 ± 0.8	40.8 ± 0.8	-867.5 ± 0.4	109.8 ± 3.9	N/A
45.6FAU	14.7 ± 1.1	32.8 ± 1.1	-871.9 ± 0.8	176.1 ± 4.0	N/A
MoO_3/2.9FAU	47.2 ± 1.7	61.1 ± 1.8	-849.1 ± 1.0	75.6 ± 3.8	-334.3 ± 102.7
MoO_3/16.1FAU	20.8 ± 1.2	38.0 ± 1.2	-891.8 ± 0.6	107.9 ± 1.7	-95.7 ± 7.5
MoO_3/29.3FAU	18.2 ± 0.5	34.3 ± 0.5	-897.8 ± 0.3	99.4 ± 2.9	-242.8 ± 4.8
MoO_3/45.6FAU	17.0 ± 1.4	32.8 ± 1.4	-896.3 ± 0.7	98.5 ± 3.9	-159.8 ± 15.4

($\Delta H_{f,el}$) at 25 °C are listed in **Table 4** . We corrected the energetic effects of hydration using dehydration enthalpies ($\Delta H_{deh,l}$) obtained from thermal analyses. $\Delta H_{f,ox}$ is plotted as a function of Si/Al ratio in **Figure 10** . Overall, the $\Delta H_{f,ox}$ of FAU frameworks without MoO_3 confined are endothermic, ranging from 69.7 ± 4.1 kJ/mol per TO_2 for 2.9FAU, to 32.8 ± 1.1 kJ/mol per TO_2 for 45.6FAU. The positive $\Delta H_{f,ox}$ values suggest the FAU samples are energetically less stable compared with their dense phase assemblages from constituent oxides, Al_2O_3 and SiO_2 (see the thermochemical cycle in **Table 2**). As the Si/Al ratio increases, $\Delta H_{f,ox}$ of empty FAU framework becomes less endothermic, exhibiting an exponential trend which gradually levels until reaching about 30 kJ/mol per TO_2 (see **Figure 10**). This trend is consistent with the formation[1-2] thermodynamics of homogeneous acid – base ternary oxide, as seen in earlier studies on various ion-exchanged zeolites. [25,26,31,37-39] On the other hand, encapsulation of MoO_3 energetically stabilizes FAU, supported by the less endothermic formation enthalpy of each MoO_3/FAU compared with corresponding FAU, ranging from 61.1 ± 1.8 kJ/mol per TO_2 for MoO_3/2.9FAU to 32.8 ± 1.4 kJ/mol per $TO_2$for MoO_3/45.6FAU. In other words, FAU framework applies strong interactions on encapsulated MoO_3 particles through surface binding and confinement effects, which pays for the "energetic of being subnano-small". Parallelly, $\Delta H_{f,el}$ mimics the trend of $\Delta H_{f,ox}$ (see **Table 4**).

The enthalpies of MoO_3 – FAU interactions, ΔH_{inter} kJ/mol per MoO_3, were calculated to quantify the magnitudes of energetic effects of formation of MoO_3/FAU with encapsulated MoO_3clusters/particles from bulk MoO_3 and empty FAU (see**Table 2** for calculation). All $\Delta H_{inter}$are exothermic between -95.7 ± 7.5 kJ/mol per MoO_3 for MoO_3/16.1FAU and -334 ± 102.7 kJ/mol per MoO_3 for MoO_3/2.9FAU. The magnitudes of ΔH_{inter} strongly suggest energetically favorable MoO_3 – FAU guest – host interactions. Despite the wide error bar, which is due to its high degree of hydration, the most exothermic ΔH_{inter} was observed on for MoO_3/2.9FAU, which mirrors the significant energetic cost to stabilize the well-dispersed metastable amorphous MoO_3 clusters, while the energetically least favorable interactions were observed for MoO_3/16.1FAU, which has nanocrystalline MoO_3 particles that lower the total energies through exothermic crystallization process as seen in our earlier study on confinement of organic nanocrystals.[35] Moreover, we would like to highlight that the ΔH_{inter} is more exothermic than what was observed for confinement of rigid organic molecules in mesoporous silicas.[35] This is owing to the strong confinement effects applied by the microporosity of zeolite Y, and the strong MoO_3 – FAU interfacial bonding. Thus, integration of these two types of strong interactions energetically stabilize the highly dispersed MoO_3 clusters, and is a prerequisite ensuring their activity, selectivity, and stability as the catalytic sites in CH_4 carburization to synthesize C_6H_6, as demonstrated by Gao *et. al.* in their kinetic, spectroscopic and computational investigations.[50,55] From a thermodynamic perspective, we anticipate that the fundamental knowledge enabled in this study will potentially benefit the chemical engineering society by revealing the energetics–structure–functionality relationships, and by providing quantitative benchmarking data for machine learning and simulation that may lead to predictive design, synthesis and processing of supported heterogeneous catalytic materials.

Conclusions

In this study, the thermodynamics of MoO_3 encapsulated in zeolite Y with different Si/Al ratios was investigated using calorimetry integrated with spectroscopic and structural methods, and catalytic performance tests, in which we successfully elucidated the energetic landscape of MoO_3/FAU catalysts, phase transition of subnano MoO_3 clusters/particles under zeolite Y confinement, and the thermodynamics–catalytic functionality relationships. In sum, the phase transition, particle dispersion, and catalytic performance of these MoO_3/FAU catalytic materials are tightly governed by the formation energetics of MoO_3/FAU and the magnitudes of MoO_3 – FAU interactions, which are functions of Si/Al ratio. Documentation of systematic experimental thermodynamic data on zeolite-based heterogeneous catalysts with encapsulated metal, oxides and carbides particles will aid chemical engineers and materials chemists for rational development of advanced catalytic materials using earth-abundant elements for a sustainable future.

Acknowledgements

This study is dedicated to a friend and colleague of Di Wu, Prof. Chia-Kuang (Frank) Tsung, Associate Professor of Chemistry at Boston College, who passed away on January 5, 2021 from complications due to

COVID-19. Di Wu thanks Profs. Alexandra Navrotsky, Bruce C. Gates, Stacey I. Zones, Gang-yu Liu, Ricardo H. R. Castro and Roland Faller. for their guidance during his Ph.D. education and postdoctoral training. Di Wu also thanks Prof. James N. Petersen and the WSU colleagues for the exceptionally strong support during his junior faculty stage. This work was supported by institutional funds from the Gene and Linda Voiland School of Chemical Engineering and Bioengineering and Alexandra Navrotsky Institute for Experimental Thermodynamics at Washington State University. Xianghui Zhang was supported by Chambroad Distinguished Scholarship. Cody B. Cockreham received support from the Achievement Rewards for College Scientists (ARCS) Fellowship from the ARCS Seattle Chapter. Vitaliy G. Goncharov and Xiaofeng Guo acknowledge the support by the institutional funds from the Department of Chemistry and the U.S. Department of Energy, Office of Nuclear Energy, grant DE-NE0008582. Portions of this research were also supported by collaboration, services, and infrastructure through the Nuclear Science Center User Facility at WSU.

Literature Cited

1. Serna P, Gates BC. Molecular Metal Catalysts on Supports: Organometallic Chemistry Meets Surface Science. *Acc. Chem. Res.*2014; 47 (8): 2612–2620. https://doi.org/10.1021/ar500170k.
2. Guan E, Ciston J, Bare SR, Runnebaum RC, Katz A, Kulkarni A, Kronawitter AX, Gates BC. Supported Metal Pair-Site Catalysts.*ACS Catal.* 2020; 10 (16): 9065–9085. https://doi.org/10.1021/acscatal.0c02000.
3. Wang H, Wang L, Xiao F. Metal@Zeolite Hybrid Materials for Catalysis.*ACS Cent. Sci.* 2020; 6 (10): 1685–1697. https://doi.org/10.1021/acscentsci.0c01130.
4. Grundner S, Markovits M, Li G *et. al.* Single-site Trinuclear Copper Oxygen Clusters in Mordenite for Selective Conversion of Methane to Methanol. *Nat. Comm.* 2015; 6: 7546. https://doi.org/10.1038/ncomms8546.
5. Wang H, Wang L, Lin D *et. al.* Strong Metal–Support Interactions on Gold Nanoparticle Catalysts Achieved through Le Chatelier's Principle. *Nat. Catal.* 2021; *in press* . https://doi.org/10.1038/s41929-021-00611-3.
6. Zhang C, Chen C, Dong H, Shen J-R, Dau H, Zhao J. Identification of Molybdenum Oxide Nanostructures on Zeolites for Natural Gas Conversion. *Science* . 2015; 348 (6235): 686–690. https://doi.org/10.1126/science.aaa7048.
7. Sushkevich VL, Palagin D, Ranocchiari M, van Bokhoven JA. Selective Anaerobic Oxidation of Methane Enables Direct Synthesis of Methanol.*Science* . 2017; 356 (6337): 523–527. https://doi.org/10.1126/science.aam9035.
8. Jin Z, Wang L, Zuidema E, Mondal K, Zhang M, Zhang J, Wang C, Meng X, Yang H, Mesters C, Xiao F. Hydrophobic Zeolite Modification for*in situ* Peroxide Formation in Methane Oxidation to Methanol.*Science* . 2020; 367 (6474): 193–197. https://doi.org/10.1126/science.aaw1108.
9. Therrien AJ, Hensley AJR, Marcinkowski MD, Zhang R, Lucci FR, Coughlin B, Schilling AC, McEwen J-S, Sykes ECH. An atomic-scale View of Single-site Pt Catalysis for Low-temperature CO Oxidation. *Nat. Catal.* 2018; 1: 192–198. https://doi.org/10.1038/s41929-018-0028-2.
10. Jones J, Xiong H, DeLaRiva AT, Peterson EJ, Pham H, Challa SR, Qi G, Oh S, Wiebenga MH, Hernández XIP, Wang Y, Datye A K. Thermally Stable Single-atom Platinum-on-Ceria Catalysts via Atom Trapping.*Science* . 2020; 353 (6295): 150–154. https://doi.org/10.1126/science.aaf8800.
11. Xiang Y, Kruse N. Tuning the catalytic CO Hydrogenation to Straight- and Long-chain Aldehydes/Alcohols and Olefins/Paraffins. *Nat. Commun.* 2017; 7: 13058. https://doi.org/10.1038/ncomms13058.
12. Zhang S, Huang ZQ, Ma Y. *et. al.* Solid Frustrated-Lewis-Pair Catalysts Constructed by Regulations on Surface Defects of Porous Nanorods of CeO_2. *Nat. Commun.* 2017; 8: 15266. https://doi.org/10.1038/ncomms15266.
13. Yang Z, Li H, Zhou H, Wang L, Wang L, Zhu Q, Xiao J, Meng X, Chen J, and Xiao F. Coking-Resistant Iron Catalyst in Ethane Dehydrogenation Achieved through Siliceous Zeolite Modulation. *J. Am. Chem. Soc.* 2020; 142 (38): 16429–16436. https://doi.org/10.1021/jacs.0c07792.

14. Zhu J, Osuga R, Ishikawa R, Shibata N, Ikuhara Y, Kondo JN, Ogura M, Yu J, Wakihara T, Liu Z, Okubo T. Ultrafast Encapsulation of Metal Nanoclusters into MFI Zeolite in the Course of Its Crystallization: Catalytic Application for Propane Dehydrogenation. *Angew. Chem. Int. Ed.* 2020; 59 (44): 19669–19674. https://doi.org/10.1002/anie.202007044.
15. Iida T, Shetty M, Murugappan K, Wang Z, Ohara K, Wakihara T, Romań-Leshkov Y. Encapsulation of Molybdenum Carbide Nanoclusters inside Zeolite Micropores Enables Synergistic Bifunctional Catalysis for Anisole Hydrodeoxygenation. *ACS Catal.* 2017; 7 (12): 8147–8151. https://doi.org/10.1021/acscatal.7b03175.
16. Liu, W., You, W., Sun, W. *et. al.* Ambient-pressure and Low-temperature Upgrading of Lignin Bio-oil to Hydrocarbons using a Hydrogen Buffer Catalytic System. *Nat Energy* . 2020; 5: 759–767. https://doi.org/10.1038/s41560-020-00680-x.
17. Zhang T. Taking on All of the Biomass for Conversion. *Science* . 2020; 367 (6484): 1305–1306. https://doi.org/10.1126/science.abb1463.
18. Zhang X, Chaudhary N, Hawkins MR *et. al.* Determining the Hydration Energetics on Carbon-Supported Ru Catalysts: An Adsorption Calorimetry and Density Functional Theory Study. *Catal. Today*2021; 365 (1): 172–180. https://doi.org/10.1016/j.cattod.2020.09.021.
19. Ding K, Gulec A, Johnson AM *et. al.* Identification of Active Sites in CO Oxidation and Water-Gas Shift over Supported Pt Catalysts.*Science.* 2015; 350 (6257): 389–393. https://doi.org/10.1126/science.aac6368.
20. Yao S, Zhang X, Zhou W *et. al.* Atomic-layered Au Clusters on α-MoC as Catalysts for the Low-temperature Water-Gas Shift Reaction.*Science.* 2017; 357 (6349): 189–192. https://doi.org/10.1126/science.aah4321.
21. Navrotsky A, Lilova K, Wu D, Asta M. Thermodynamics of Complex Solids.*J. Mater. Res.* 2019; 34 (19): 3241–3242. https://doi.org/10.1557/jmr.2019.300.
22. Davis ME, Lobo RF. Zeolite and Molecular Sieve Synthesis. *Chem. Mater.* 1992; 4 (4): 756–768. https://doi.org/10.1021/cm00022a005.
23. Navrotsky A, Trofymluk O, Levchenko A A. Thermochemistry of Microporous and Mesoporous Materials. *Chem. Rev.* 2009; 109 (9): 3885–3902. https://doi.org/10.1021/cr800495t.
24. Petrovic I, Navrotsky A, Davis ME, Zones SI. Thermochemical Study of the Stability of Frameworks in High Silica Zeolites. *Chem. Mater.* 1993; 5 (12): 1805–1813. https://doi.org/10.1021/cm00036a019.
25. Hu Y, Navrotsky A, Chen CY, Davis ME. Thermochemical Study of the Relative Stability of Dense and Microporous Aluminophosphate Frameworks. *Chem. Mater.* 1995; 7 (10): 1816–1823. https://doi.org/10.1021/cm00058a010.
26. Petrovic I, Navrotsky A. Thermochemistry of Na-Faujasites with Varying Si/Al Ratios. *Microporous Mater.* 1997; 9 (1–2): 1–12. https://doi.org/10.1016/S0927-6513(96)00060-0.
27. Piccione PM, Laberty C, Yang S, Camblor MA, Navrotsky A, Davis ME. Thermochemistry of Pure-Silica Zeolites. *J. Phys. Chem. B.*2000; 104 (43): 10001–10011. https://doi.org/10.1021/jp002148a.
28. Piccione PM, Woodfield BF, Boerio-Goates J, Navrotsky A, Davis ME. Entropy of Pure-Silica Molecular Sieves. *J. Phys. Chem. B.*2001; 105 (25): 6025–6030. https://doi.org/10.1021/jp010491p.
29. Piccione PM, Yang S, Navrotsky A, Davis ME. Thermodynamics of Pure-silica Molecular Sieve Synthesis. *J. Phys. Chem. B* 2002; 106 (14): 3629–3638. https://doi.org/10.1021/jp014427j.
30. Yang S, Navrotsky A, Phillips BL. *In Situ* Calorimetric, Structural, and Compositional Study of Zeolite Synthesis in the System $5.15Na_2O$-$1.00Al_2O_3$-$3.28SiO_2$-$165H_2O$.*J. Phys. Chem. B.* 2000; 104 (25): 6071–6080. https://doi.org/10.1021/jp9944278.
31. Yang S, Navrotsky A. Energetics of Formation and Hydration of Ion-exchanged Zeolite Y. *Microporous Mesoporous Mater.* 2000; 37 (1–2): 175–186. https://doi.org/10.1016/S1387-1811(99)00264-4.
32. Yang S, Navrotsky A, Wesolowski DJ, Pople JA. Study on Synthesis of TPA-Silicalite-1 from Initially Clear Solutions of Various Base Concentrations by *In Situ* Calorimetry, Potentiometry, and SAXS.*Chem. Mater.* 2004; 16 (2): 210-219. https://doi.org/10.1021/cm030587r.
33. Yang S, Navrotsky A. Early-Stage Reactions in Synthesis of TPA-Silicalite-1: Studies by *In Situ* Calorimetry, SAXS, and pH Measurements. *Chem. Mater.* 2004; 16 (19): 3682-3687.

https://doi.org/10.1021/cm035272q.
34. Yang S, Navrotsky A. *In Situ* Calorimetric Study of the Growth of Silica TPA-MFI Crystals from an Initially Clear Solution. *Chem. Mater.* 2002; 14 (6): 2803-2811. https://doi.org/10.1021/cm0200689.
35. Wu D, Hwang SJ, Zones SI, Navrotsky A. Guest – Host Interactions of a Rigid Organic Molecule in Porous Silica Frameworks. *Proc. Natl. Acad. Sci. USA.* 2014; 111 (5): 1720-1725. https://doi.org/10.1073/pnas.1323989111.
36. Sun H, Wu D, Guo X, Shen B, Liu J, Navrotsky A. Energetics of Confinement of Hexane in Ca – Na Ion Exchanged Zeolite A. *J. Phys. Chem. C* 2014; 118 (44): 25590-25596. https://doi.org/10.1021/jp508514e.
37. Sun H, Wu D, Guo X, Shen B, Navrotsky A. Energetics and Structural Evolution of Na – Ca Exchanged Zeolite A during Heating. *Phys. Chem. Chem. Phys.* 2015; 17, 9241-9247. https://doi.org/10.1039/c5cp00016e.
38. Sun H, Wu D, Guo X, Shen B, Navrotsky A. "Energetics of Sodium – Calcium Exchanged Zeolite A", *Phys. Chem. Chem. Phys.* 2015; 17, 11198-11203. https://doi.org/10.1039/c5cp01133g.
39. Sun H, Wu D, Liu K, Guo X, Navrotsky A. Energetics of Alkali and Alkaline Earth Ion-exchanged Zeolite A. *J. Phys. Chem. C* 2016; 120 (28): 15251-15256. https://doi.org/10.1021/acs.jpcc.6b04840.
40. Yang S, Guo X, Verma A, Shiflett MB, Corbin DR, Navrotsky A. Thermochemical Insights into Stability and Hydration of Ion-Exchanged Zeolite ZK-5 (KFI Framework). *J. Phys. Chem. C.* 2020; 124 (48): 26193–26202. https://doi.org/10.1021/acs.jpcc.0c06796.
41. Zones SI. Jayanthi K, Pascual J, Xie D, Navrotsky A. Energetics of the Local Environment of Structure-Directing Agents Influence Zeolite Synthesis. *Chem. Mater.* 2021; 33 (6) 2126–2138. https://doi.org/10.1021/acs.chemmater.0c04796.
42. Zhang X, Cockreham CB, Huang Z, Sun H, Yang C, Marin-Flores OG, *et. al.* Thermodynamics of Water-Cationic Species-Framework Guest-Host Interactions within Transition Metal Ion-Exchanged Mordenite Relevant to Selective Anaerobic Oxidation of Methane to Methanol. *J. Phys. Chem. Lett.* 2020; 11 (12): 4774–4784. https://doi.org/10.1021/acs.jpclett.0c01331.
43. Navrotsky A. Progress and New Directions in Calorimetry: A 2014 Perspective. *J. Am. Ceram. Soc.* 2014; 97 (11): 3349–3359. https://doi.org/10.1111/jace.13278.
44. Sang S, Liu Z, Tian P, Liu Z, Qu L, Zhang Y. Synthesis of Small Crystals Zeolite NaY. *Mater. Lett.* 2006; 60 (9–10): 1131–1133. https://doi.org/10.1016/j.matlet.2005.10.110.
45. Holmberg BA, Wang H, Yan Y. High Silica Zeolite Y Nanocrystals by Dealumination and Direct Synthesis. *Microporous Mesoporous Mater.* 2004; 74 (1–3): 189–198. https://doi.org/10.1016/j.micromeso.2004.06.018.
46. Janssen AH, Koster AJ, De Jong KP. Three-dimensional Transmission Electron Microscopic Observations of Mesopores in Dealuminated Zeolite Y. *Angew. Chem. Int. Ed.* 2001; 40 (6):1102–1104. https://doi.org/10.1002/1521-3773(20010316)40:6%3C1102::AID-ANIE11020%3E3.0.CO;2-6.
47. De Jong KP, Zečević J, Friedrich H, De Jongh PE, Bulut M, Van Donk S, *et. al.* Zeolite Y Crystals with Trimodal Porosity as Ideal Hydrocracking Catalysts. *Angew. Chem. Int. Ed.* 2010; 49 (52): 10074–10078. https://doi.org/10.1002/ange.2010043.
48. Bordiga S, Regli L, Lamberti C, Zecchina A, Bjørgen M, Lillerud KF. FTIR Adsorption Studies of H_2O and CH_3OH in the Isostructural H-SSZ-13 and H-SAPO-34: Formation of H-bonded Adducts and Protonated Clusters. *J. Phys. Chem. B.* 2005; 109 (16): 7724–7732. https://doi.org/10.1021/jp044324b.
49. Zecchina A, Geobaldo F, Spoto G, Bordiga S, Ricchiardi G, Buzzoni R, *et. al.* FTIR Investigation of the Formation of Neutral and Ionic Hydrogen-bonded Complexes by Interaction of H-ZSM-5 and H-mordenite with CH_3CN and H_2O: Comparison with the H-NAFION Superacidic System. *J. Phys. Chem.*1996; 100 (41): 16584–16599. https://doi.org/10.1021/jp960433h.
50. Gao J, Zheng Y, Fitzgerald GB, De Joannis J, Tang Y, Wachs IE, *et. al.* Structure of Mo_2C_x and Mo_4C_x Molybdenum Carbide Nanoparticles and Their Anchoring Sites on ZSM-5 Zeolites. *J. Phys. Chem. C.*2014; 118 (9): 4670–4679. https://doi.org/10.1021/jp4106053.
51. Wang D, Lunsford JH, Rosynek MP. Characterization of a Mo/ZSM-5 Catalyst for the Conversion of Methane to Benzene. *J. Catal.*1997; 169(1): 347–358. https://doi.org/10.1006/jcat.1997.1712.

52. Lee EL, Wachs IE. *In Situ* Spectroscopic Investigation of the Molecular and Electronic Etructures of SiO_2 Supported Surface Metal Oxides. *J. Phys. Chem. C* . 2007;111(39):14410–14425. https://doi.org/10.1021/jp0735482.
53. Lee EL, Wachs IE. Molecular Design and *in situ* Spectroscopic Investigation of Multilayered Supported $M_1O_x/M_2O_x/SiO_2$Catalysts. *J. Phys. Chem. C.* 2008; 112 (51): 20418–20428. https://doi.org/10.1021/jp805265m.
54. Tian H, Roberts CA, Wachs IE. Molecular Structural Determination of Molybdena in Different Environments: Aqueous Solutions, Bulk Mixed Oxides, and Supported MoO_3 Catalysts. *J. Phys. Chem. C.* 2010; 114 (33): 14110–14120. https://doi.org/10.1021/jp103269w.
55. Zheng Y, Tang Y, Gallagher JR, Gao J, Miller JT, Wachs IE, Podkolzin SG. Molybdenum Oxide, Oxycarbide, and Carbide: Controlling the Dynamic Composition, Size, and Catalytic Activity of Zeolite- Supported Nanostructures. *J. Phys. Chem. C.* 2019; 123 (36): 22281–22292https://doi.org/10.1021/acs.jpcc.9b05449.
56. Okemoto A, Harada MR, Ishizaka T, Hiyoshi N, Sato K. Catalytic Performance of MoO_3/FAU Zeolite Catalysts Modified by Cu for Reverse Water Gas Shift Reaction. *Appl. Catal. A Gen.*2020; 117415. https://doi.org/10.1016/j.apcata.2020.117415.
57. Liu H, Xu Y. H_2-TPR Study on Mo/HZSM-5 Catalyst for CH_4 Dehydroaromatization. *Chinese J. Catal.*2006; 27 (4): 319–323. https://doi.org/10.1016/S1872-2067(06)60020-X.
58. Zhao K, Jia L, Wang J, Hou B, Li D. The Influence of the Si/Al Ratio of Mo/HZSM-5 on Methane Non-oxidative Dehydroaromatization. *New J. Chem.* 2019; 43(10): 4130–4136. https://doi.org/10.1039/C9NJ00114J.
59. Kosinov N, Uslamin EA, Coumans FJAG, Wijpkema ASG, Rohling RY, Hensen EJM. Structure and Evolution of Confined Carbon Species during Methane Dehydroaromatization over Mo/ZSM-5. *ACS Catal.* 2018; 8 (9): 8459–8467. https://doi.org/10.1021/acscatal.8b02491.
60. Brezesinski T, Wang J, Tolbert SH, Dunn B. Ordered Mesoporous ∝-MoO_3 with Iso-oriented Nanocrystalline Walls for Thin-film Pseudocapacitors. *Nat. Mater.* 2010; 9: 146–151 (2010). https://doi.org/10.1038/nmat2612.
61. Cid R, Llambías FJG, Fierro JLG, Agudo AL, Vlllaseñor J. Physicochemical Characterization of MoO_3-NaY Zeolite Catalysts. *J. Catal.* 1984; 89 (2): 478–488. https://doi.org/10.1016/0021-9517(84)90324-5.
62. Spevack PA, McIntyre NS. Thermal Reduction of Molybdenum Trioxide. *J. Phys. Chem.* 1992; 96 (22): 9029–9035. https://doi.org/10.1021/j100201a062.
63. Robie RA, Hemingway BS. Thermodynamic Properties of Minerals and Related Substances at 298.15 K and 1 Bar (10^5Pascals) Pressure and Higher Temperatures. U.S. Government Printing Office, Washington D.C., U.S. 1995. https://doi.org/10.3133/b2131.